

Out-of-plane polarization and topological magnetic vortices in multiferroic CrPSe₃

Weiwei Gao,^{1,2} Jijun Zhao,^{1,3,*} and James R. Chelikowsky^{2,4,5,†}

¹Key Laboratory of Materials Modification by Laser,
Ion and Electron Beams, Ministry of Education,

Dalian University of Technology, Dalian 116024, China

²Center for Computational Materials, Oden Institute for Computational Engineering and Sciences,
The University of Texas at Austin, Austin, TX 78712

³School of Physics, Dalian University of Technology

⁴Department of Physics, The University of Texas at Austin, Austin, TX 78712

⁵McKetta Department of Chemical Engineering, The University of Texas at Austin, Austin, TX 78712

Two-dimensional (2D) multiferroic materials are ideal systems for exploring new coupling mechanisms between different ferroic orders and producing novel quantum phenomena with potential applications. We employed first-principles density functional theory calculations to discover intrinsic ferroelectric and anti-ferroelectric phases of CrPSe₃, which show ferromagnetic order and compete with the centrosymmetric phase with an antiferromagnetic order. Our analysis shows that the electrical dipoles of such type-I multiferroic phases come from the out-of-plane displacements of phosphorus ions due to the stereochemically active lone pairs. The coupling between polar and magnetic orders creates the opportunity for tuning the magnetic ground state by switching from the centrosymmetric to the ferroelectric phase using an out-of-plane electric field. In ferroelectric and antiferroelectric phases, the combination of easy-plane anisotropy and Dzyaloshinskii-Moriya interactions (DMI) indicate they can host topological magnetic vortices like meron pairs.

Multiferroic systems concomitantly host two or more ferroic orders and promise novel applications by coupling different order parameters and supporting exotic quantum states [1]. In particular, intrinsic magnetoelectric multiferroics, such as BiFeO₃ and YMnO₃, are of special interest not only because they are model systems for understanding magnetoelectric coupling, but also because they have unusual features like conductive domain walls [2–4] and photostriction [5, 6]. As different ferroic ordering [7–11] have recently been found in 2D materials, researchers are devoting more attention to 2D multiferroic systems [12]. However, intrinsic bulk magnetoelectrics, let alone 2D magnetoelectrics, are difficult to find owing to the contradicting requirements for chemical conditions supporting ferroelectricity and magnetism [13].

Recently, artificial 2D multiferroic systems have been proposed, which involve combining materials with diverse ferroic orders to generate heterostructures [14], doping magnetic ions into ferroelectrics [15], or creating bilayer structures with customized stacking orders [16]. Theoretically, a few intrinsic 2D magnetoelectrics have also been predicted. For example, Zhang *et al.* proposed a type-II multiferroic MXene with weak electric dipole moments induced by the helical magnetic order [17]. Qi *et al.* discovered that a class of monolayer quaternary compounds has an anti-ferroelectric ground-state structure combined with long-range magnetism [18]. Several groups predicted that monolayer VOX₂ (X = Cl, Br, I) will have magnetic ordering as well as in-plane ferroelectricity [19, 20]. In monolayer VOI₂, the combination of iodine’s strong spin-orbital coupling and breaking inversion symmetry causes large DMI [21, 22] and topological magnetic vortices [19]. Meanwhile, there are still debates in the literature about the metallicity of VOI₂, which hinders its in-plane fer-

roelectricity [23]. Experiments have yet to corroborate these pioneering predictions of intrinsic 2D multiferroics.

In this Letter, we revisit the layered Van der Waals material CrPSe₃ using first-principles calculations and Monte-Carlo simulations. Our study reveals unexpected ferroelectric and anti-ferroelectric phases which have ferromagnetic orders and compete with the centrosymmetric phase, which is antiferromagnetic. The coupling between magnetic ground states and polar orders sheds light on tuning magnetism using electric field. In addition, the polar and anti-polar phases also display sizable DMI and easy-plane anisotropy, which support the formation of topological magnetic vortices such as merons [24].

CrPSe₃ belongs to the MPX₃ family of metal thio- and selenophosphites, where M stands for transition metal elements and X for sulfur or selenium [25]. Most MPX₃, including CrPSe₃, have layered structures stabilized by Van der Waals interactions, but they appear in various stacking orders. To investigate the structure and magnetic order of CrPSe₃, we performed density functional theory (DFT) calculations based on a plane-wave pseudopotential framework [26, 27]. When comparing various exchange-correlation functionals [28, 29], we found PBEsol and local-density approximation functionals provide a better overall description of the structural properties of bulk CrPSe₃ (as shown in Supplementary materials [30][31–33]). Here all results presented were calculated with the PBEsol functional.

We carried out DFT+U calculations [34] with effective parameters U_{eff} to optimize the structure and determine the energy of monolayer and bulk CrPSe₃ [25]. Interestingly, in addition to the centrosymmetric phase similar to other MPX₃, we found an unexpected polar phase with phosphorus ions tilting along the out-of-plane direction.

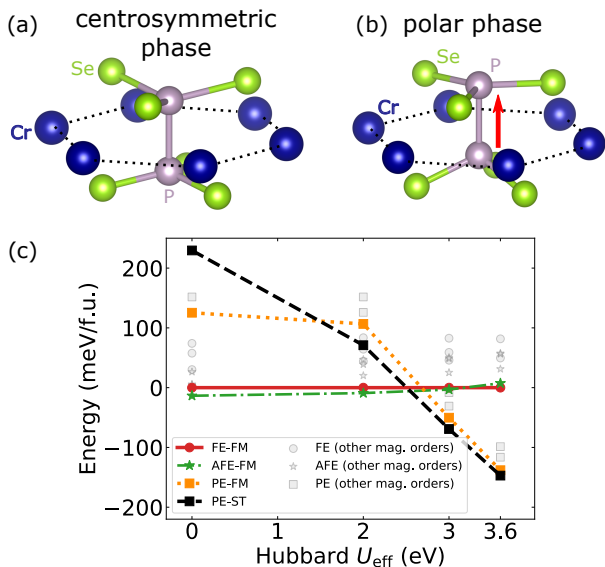


Figure 1. Atomic models for (a) the centrosymmetric phase and (b) the polar phase [35]; (c) Comparison of the total energies between different multiferroic configurations when calculated with different U_{eff} .

The displacements of phosphorus ions break the inversion symmetry, as schematically depicted in Fig. 1 (b). Furthermore, an anti-polar structure can be constructed based on the polar phase, in which the phosphorus atoms in neighboring cells tilt in opposing directions (see Supplementary material for a plot of the anti-polar structure).

To comprehensively compare the energies of various structures and magnetic orders of monolayer CrPSe₃, we examined 12 different multiferroic configurations which combine polar (FE), anti-polar (AFE), centrosymmetric (i.e., paraelectric or PE) structures with the FM and three common antiferromagnetic orders, namely, zigzag (ZZ), stripy (ST), and Néel (NL) orders. Acronyms are used to represent multiferroic phases in the following discussions. “FE-FM”, for example, denotes the phase with the polar structure and a ferromagnetic order. As shown in Fig. 1 (c), the energies of 12 configurations are compared with the energy of the FE-FM phase, which is set as the reference point. Overall, the energies of the PE phases change with U_{eff} at a different rate compared to the AFE and FE phases. The difference is attributed to different electron occupations of the Cr *3d*-orbitals (i.e., different oxidation states of Cr atoms) in polar and non-polar structures. For a reasonable range of $U_{\text{eff}} \in [2.0, 3.0]$ eV of Cr [36], the FE-FM, AFE-FM, and PE-ST phases are competing phases with similar energies. The competition between AFE-FM, FE-FM, and PE-ST phases of CrPSe₃ suggest the possibility of the coexistence of these three phases. Similar competitions between various phases has also been observed in ferroelectrics such as In₂Se₃ [37], CuInP₂Se₆ [38], and so on [39–41].

Among different multiferroic configurations, the AFE-

FM phase has the lowest energy when $U_{\text{eff}} < 2.5$ eV, while PE-ST is the lowest when $U_{\text{eff}} > 2.5$ eV, as shown in Fig. 1 (c). The AFE-FM and FE-FM phases have small energy differences within 12 meV/f.u. As U_{eff} rises over 3.2 eV, the energy of FE-FM phase falls below that of AFE-FM phase. Examining the magnetic orders, we find FM order remains the lowest-energy magnetic order for both the FE and AFE structures. When $U_{\text{eff}} > 1.5$ eV, the PE phase has the ST magnetic order, which changes to the FM order when U_{eff} is lower than 1.5 eV. When U_{eff} is set to 0, which is an improper value for Cr, the predicted magnetic order of the PE structure is the FM order, which matches prior work [42] utilizing the PBE+D2 method [43]. We also conducted PBE+D2 [29] computations, which quantitatively agree with earlier results for these magnetic ordering [42], reinforcing the reproducibility of our work.

Using a frozen-phonon method [44], we computed the phonon spectra of the polar (as shown in Fig. 2 (a)), centrosymmetric, and antipolar structures. Their phonon dispersions show no imaginary frequency modes and demonstrate dynamical stability. Our Berry-phase calculations [45] show the polar phase has an electric polarization density of 3.98 pC/m, which is larger than the predicted type-II multiferroic Hf₂VC₂F₂ (1.98 pC/m) [17]. The nudged-elastic band (NEB) approach is adopted to determine the energy barrier $E^{P \rightarrow -P}$ of collectively reversing the electric polarization direction [46]. The switching energy barrier $E^{P \rightarrow -P}$ changes from 0.05 to 0.13 eV/f.u. when U_{eff} varies from 3.0 eV to 2.0 eV. When the U_{eff} is set to a value greater than 2.4 eV, a local minimum similar to the PE phase appears in the middle of the transition path, as shown in Fig. 2 (b). The energy barrier to leave the potential well around the local minimum structure, however, is reasonably low (less than 100 meV/f.u. for $U_{\text{eff}} < 3.0$ eV) to permit a switching of polarization under suitable electric field, as it is comparable to other out-of-plane 2D ferroelectrics [47, 48]. Notably, the interdependence between the polar and magnetic order in CrPSe₃ is uncommon and offers an opportunity for altering magnetic ground-states by inducing a transition from the centrosymmetric structure to the polar structure.

Similarly, we estimated the energy barrier $E^{\text{FE} \rightarrow \text{AFE}}$ between the FE-FM and AFE-FM phases. The energy profile of transitioning from the FE-FM phase to the AFE-FM phase is shown in Fig. 2 (c). There are two energy barriers along the transition path. The crystal structure transforms into an intermediate configuration close to the PE phase after passing through the first energy barrier. The intermediate configuration corresponds to the dip on energy curve of the switching process, as shown in Fig. 2 (c). After overcoming the second barrier, the structure turns into the AFE structure. Overall, the heights of these two barriers are on the order of 40 meV/f.u., which is in the same order-of-magnitude as the energy barrier $E^{P \rightarrow -P}$ of switching the polarization of the FE

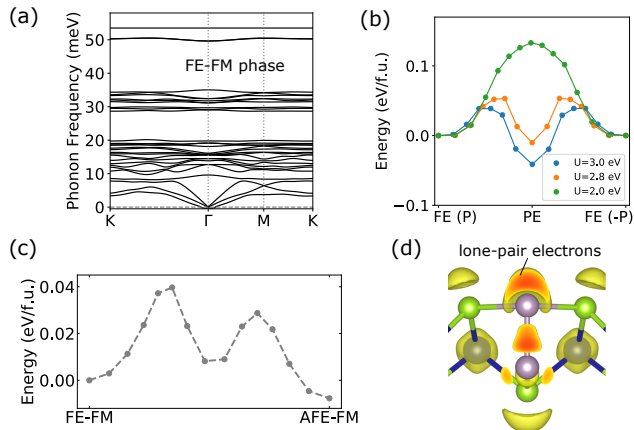


Figure 2. (a) Phonon dispersion of the FE-FM phase; (b) Energy barriers for switching the electric polarization of the ferroelectric (i.e., polar) phase; (c) The energy profile for a structural transition from the FE-FM phase to the AFE-FM phase calculated with PBEsol+U (with $U_{\text{eff}} = 2.8$ eV); (d) Isosurfaces of electron localization function in the polar phase, showing the lone-pair electrons near phosphorus atoms.

phase. Although the FE-FM phase is metastable, the energy ordering of the FE-FM and AFE-FM phases can be reversed with moderate electric fields or strain (see the supplementary materials), suggesting the possibility of inducing a phase transition from the AFE-FM phase to the FE-FM phase using electric field or strain.

For bulk CrPSe_3 phases, we considered additional interlayer antiferroelectric and interlayer antiferromagnetic orders (see Supplementary Material for details of these two orders), and constructed 20 different multiferroic configurations. The dependence of ground-state phases on U_{eff} is similar to the situation of monolayer CrPSe_3 . As the Hubbard U_{eff} parameter changes, the lowest-energy configuration is the PE-ST phase when U_{eff} parameter is between around 2.6 to 3.6 eV, but changes to the AFE-FM phase when U_{eff} drops to below 2.6 eV. With U_{eff} larger than 2.0 eV, our calculation results show that the ground-state magnetic order of the centrosymmetric phase is anti-ferromagnetic ST ordering. Recently, a theoretical study shows that monolayer and bulk PE phase of CrPSe_3 have NL order, while the ST order has an energy slightly higher than the NL order [49]. The discrepancy between this work and our study likely originates from different types of pseudopotentials (see Supplementary materials for more details). Experiments show that bulk CrPSe_3 has an anti-ferromagnetic order [50], while its detailed anti-ferromagnetic spin arrangement is not determined.

Because phosphorous contributes polarization and chromium contributes magnetism, the coexistence of polar and magnetic order does not violate the d^0 -rule [13] and the FE-FM and AFE-FM phases are type-I multiferroic phases. The out-of-plane displacements of phosphorus

ions in polar and anti-polar structures are related to the oxidation states of Cr ions. In the centrosymmetric phase, the oxidation state of chromium ions are Cr^{2+} , similar as the transition metal ions M^{2+} in most MPSe_3 systems [25]. However, in the anti-polar and polar phases, it becomes Cr^{3+} . Compared to the centrosymmetric structure with Cr^{2+} , a pair of Cr^{3+} ions in the polar structures give up two electrons, generating a lone pair located nearby phosphorus atoms. As a result, analogous to BiFeO_3 [1], lone-pair electrons result in an asymmetric charge distribution that pushes the phosphorus atoms out of plane. The isosurface map of the electron-localization function (ELF) visualizes the position of lone pairs and the consequent structural change, as illustrated in Fig. 2 (d).

With the spin-orbit coupling effects contributed by Se atoms and the breaking local inversion symmetry, the AFE-FM and FE-FM phases can potentially show significant DMI, which can lead to topological spin textures. Here an extended Heisenberg model describing the magnetic interactions in a 2D spin-lattice is considered:

$$H = \sum_{\langle i,j \rangle} J_1 \mathbf{n}_i \cdot \mathbf{n}_j + \sum_{\langle\langle i,j \rangle\rangle} J_2 \mathbf{n}_i \cdot \mathbf{n}_j + \sum_{\langle i,j \rangle} \mathbf{D}_1 \cdot (\mathbf{n}_i \times \mathbf{n}_j) + \sum_i \sum_{\alpha=x,y,z} A_\alpha n_{i\alpha}^2$$

where \mathbf{n}_i are unit vectors; $\langle \rangle$ and $\langle\langle \rangle\rangle$ stand for nearest and next-nearest neighbors, respectively; $J_{1,2}$ are the symmetric exchange coupling and \mathbf{D}_1 is the DMI coupling; A_α describes the single-ion magnetic anisotropy. The exchange parameters are calculated using a four-states mapping method for FE-FM and AFE-FM phases [51]. Table I contains the magnetic parameters of the FE-FM phase. Details on the magnetic parameters of the AFE-FM phase are presented in the Supplementary Material. Both FE-FM and AFE-FM phase have easy-plane magnetic anisotropy and large nearest-neighbor DMI interaction \mathbf{D}_1 . The FE-FM phase retains the C_3 symmetry of the PE phases and its easy-plane anisotropy is close to the XY model. According to the Mermin-Wagner theorem [52], the FE phase does not allow long-range FM order in a perfect infinite-size crystal. In a finite-size sample of the FE-FM phase, however, weak ferromagnetism can arise. In its easy plane, the AFE-FM phase has an easy axis along y -direction, which violates the continuous $O(2)$ symmetry and allows for long-range ferromagnetic order.

Table I. Parameters (in meV) for the magnetic Hamiltonian of the FE-FM phase calculated with PBEsol+U ($U_{\text{eff}} = 2.8$ eV).

J_1	J_2	A_x	A_y	\mathbf{D}_1
-21.7	-0.75	-0.27	-0.27	[0.3, 0.0, -1.9]

Because the electric polarization for the FE-FM phase

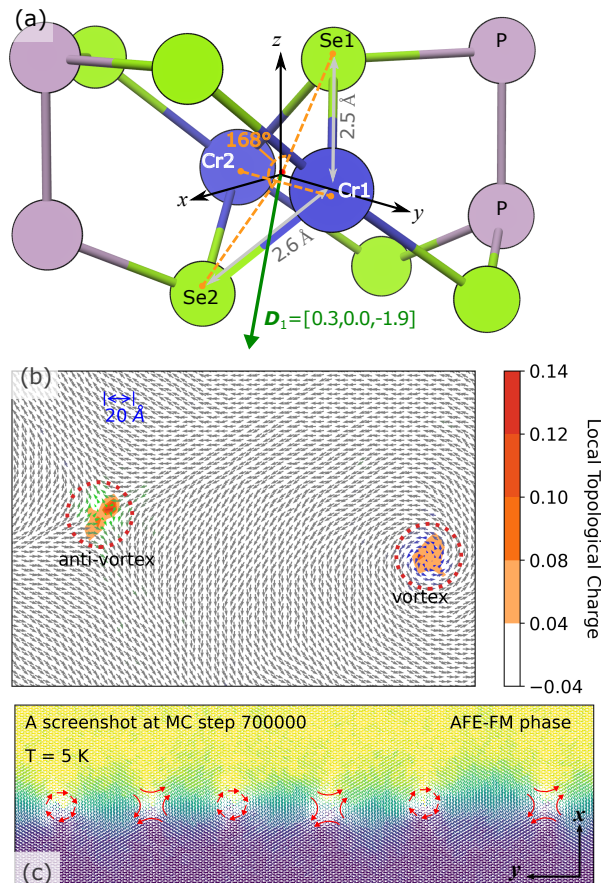


Figure 3. (a) A schematic plot showing the nearby atoms and the direction of DMI vector \mathbf{D}_1 between nearest-neighbour Cr ions; (b) A snapshot of a Monte-Carlo simulation for the FE-FM phase ($T = 2 \text{ K}$) which shows a pair of anti-merons (topological charge of $\frac{1}{2}$) with winding numbers -1 and 1 respectively. The local topological charge density is plotted with contours on the background. Spins are colored in green or blue according to out-of-plane components. (c) A screenshot for six long-lived merons of the AFE-FM phase. Spins are colored according to the direction of their in-plane components.

is out-of-plane, one could expect the DMI vector to be in-plane. Notably, our calculations reveal that the DMI vector has a significant out-of-plane component. To understand this, we consider two adjacent ions Cr1 and Cr2, as well as the middle point M of the line Cr1Cr2 connecting them. Fig. 3 (a) depict the local structure of two nearest-neighbour Cr ions. The FE-FM structure has a mirror plane passing through M and is perpendicular to Cr1Cr2. According to Moriya's rules [22], the DMI vector \mathbf{D}_1 should also be perpendicular to Cr1Cr2. Our computational results agree with these rules. The distortion of Se ions, which mediates the indirect exchange contacts between nearby Cr ions, accounts for the large out-of-plane component of \mathbf{D}_1 . In the PE phase, atoms Cr1, Cr2, Se1, and Se2 are coplanar and form a

parallelogram in the PE phase. In contrast, in the FE phase, the displacements of selenium ions make the dihedral angle $\angle Se_1Cr_1Cr_2Se_2 = 168^\circ$ and bond lengths $d_{Cr_1Se_1} \neq d_{Cr_1Se_2}$, shown in Fig. 3 (a). This local environment breaks the inversion symmetry and results in large out-of-plane components of \mathbf{D}_1 . The modest dipole field induced by the shifted phosphorous ions, on the other hand, creates a significantly smaller in-plane DMI component.

The synergy of out-of-plane DMI components and in-plane magnetic anisotropy favors the formation of meron and anti-meron pairs [19, 53] in both FE-FM and AFE-FM phases. Monte-Carlo (MC) simulations [54] of the magnetic Hamiltonian were conducted for the FE-FM and AFE-FM phases. We initialized the spin-lattice with random spin vectors and examine its evolution in MC simulations. Typically, after a few thousand MC steps, small in-plane ferromagnetic domains emerge and topologically non-trivial spin vortices and anti-vortices form on the domain boundaries. Such topologically non-trivial magnetic excitations have a topological charge of one half or negative one half, suggesting they are anti-merons or merons. Notably, merons appear even under $T = 30 \text{ K}$, which is higher than the allowed temperature range for merons to emerge in $CrCl_3$ [55] and VOI_2 [19]. Furthermore, the formation of merons is robust to the variation of DMI parameters and Heisenberg exchange parameters. Merons and anti-merons are still observed at around $T = 5 \text{ K}$ even when the magnitude of DMI vector decreases by 50%. In MC simulations, merons with winding numbers $w = 1$ and $w = -1$, which are known as vortex and anti-vortex merons, emerge in pairs, similar as in prior investigations [56, 57]. Fig. 3 (b) is a typical snapshot of MC simulations for the FE-FM phase, showing real-space spin textures and the distribution of topological charge in the spin-lattice. Clearly, the topological charge density is concentrated near merons or anti-merons. As the MC simulation progresses, vortex (anti)vortex tend to attract nearby anti-vortex (anti)merons. Such annihilation phenomenon is also observed in Landau-Lifshitz-Gilbert simulations for $CrCl_3$ [55, 56] and kagome magnets [58]. In the FE-FM phase, merons and anti-merons will all be annihilated after a long enough MC simulation (typically after 5×10^5 steps). In the AFE-FM phase, unusual long-lived vortex and anti-vortex meron pairs appears. Even after 2×10^6 MC steps, these topological excitation pairs stabilize on the boundaries of adjacent ferromagnetic domains and exhibit no tendency to annihilate each other. Three long-lived vortex-antivortex pairs are shown in Fig. 3 (c). Such long-lived merons are typically located on the domain boundaries parallel to the y or x -axis.

In all, we comprehensively investigated the structures and magnetic orders of different phases in bulk and monolayer $CrPSe_3$. We identify two multiferroic phases of $CrPSe_3$, namely a ferroelectric and an anti-ferroelectric phase with ferromagnetic orders, while the experimentally

studied centrosymmetric phases is antiferromagnetic. The multiferroic phases are both dynamically stable and compete with the centrosymmetric phase. The metastable ferroelectric phase carries an out-of-plane electric polarization and is separated from the centrosymmetric and anti-ferroelectric phase by surmountable energy barriers. The coupling between the polar order and magnetic ground state provide new opportunities for tuning magnetism through electric field. Moreover, with significant out-of-plane DMI interaction and in-plane anisotropy, the ferroelectric and anti-ferroelectric phases can potentially host magnetic topological excitations including merons and antimerons under suitable conditions. Our work suggests CrPSe₃ is a promising material for exploring intrinsic low-dimensional multiferroicity and topological magnetic excitations.

ACKNOWLEDGEMENT

WG and JRC acknowledge support from a subaward from the Center for Computational Study of Excited-State Phenomena in Energy Materials at the Lawrence Berkeley National Laboratory, which is funded by the U.S. Department of Energy, Office of Science, Basic Energy Sciences, Materials Sciences and Engineering Division under Contract No. DEAC02-05CH11231, as part of the Computational Materials Sciences Program. WG acknowledge support from the Fundamental Research Funds for the Central Universities, grant DUT21RC(3)033. WG and JZ acknowledge the support by grant 12104080 and 91961204 from National Science Foundation of China. Computational resources are provided by Shanghai supercomputer center, national energy research scientific computing center (NERSC), and the Texas advanced computing center (TACC).

* zhaojj@dlut.edu.cn

† jrc@utexas.edu

- [1] N. A. Spaldin and R. Ramesh, “Advances in magnetoelectric multiferroics,” *Nature Materials* **18**, 203–212 (2019).
- [2] S. Ghara, K. Geirhos, L. Kuerten, P. Lunkenheimer, V. Tsurkan, M. Fiebig, and I. Kézsmárki, “Giant conductivity of mobile non-oxide domain walls,” *Nature Communications* **12**, 3975 (2021).
- [3] J. Seidel, L. W. Martin, Q. He, Q. Zhan, Y.-H. Chu, A. Rother, M. E. Hawkrige, P. Maksymovych, P. Yu, M. Gajek, N. Balke, S. V. Kalinin, S. Gemming, F. Wang, G. Catalan, J. F. Scott, N. A. Spaldin, J. Orenstein, and R. Ramesh, “Conduction at domain walls in oxide multiferroics,” *Nature Materials* **8**, 229–234 (2009).
- [4] Dennis Meier, “Functional domain walls in multiferroics,” *Journal of Physics: Condensed Matter* **27**, 463003 (2015).
- [5] Tzu-Chiao Wei, Hsin-Ping Wang, Heng-Jui Liu, Dung-Sheng Tsai, Jr-Jian Ke, Chung-Lun Wu, Yu-Peng Yin, Qian Zhan, Gong-Ru Lin, Ying-Hao Chu, and Jr-Hau He, “Photostriction of strontium ruthenate,” *Nature Communications* **8**, 15018 (2017).
- [6] B. Kundys, M. Viret, D. Colson, and D. O. Kundys, “Light-induced size changes in bifeo₃ crystals,” *Nature Materials* **9**, 803–805 (2010).
- [7] Cheng Gong, Lin Li, Zhenglu Li, Huiwen Ji, Alex Stern, Yang Xia, Ting Cao, Wei Bao, Chenzhe Wang, Yuan Wang, Z. Q. Qiu, R. J. Cava, Steven G. Louie, Jing Xia, and Xiang Zhang, “Discovery of intrinsic ferromagnetism in two-dimensional van der waals crystals,” *Nature* **546**, 265–269 (2017).
- [8] Bevin Huang, Genevieve Clark, Efrén Navarro-Moratalla, Dahlia R. Klein, Ran Cheng, Kyle L. Seyler, Ding Zhong, Emma Schmidgall, Michael A. McGuire, David H. Cobden, Wang Yao, Di Xiao, Pablo Jarillo-Herrero, and Xiaodong Xu, “Layer-dependent ferromagnetism in a van der waals crystal down to the monolayer limit,” *Nature* **546**, 270–273 (2017).
- [9] Xue Jiang, Qinxi Liu, Jianpei Xing, Nanshu Liu, Yu Guo, Zhifeng Liu, and Jijun Zhao, “Recent progress on 2d magnets: Fundamental mechanism, structural design and modification,” *Applied Physics Reviews* **8**, 031305 (2021).
- [10] Yu Zhou, Di Wu, Yihan Zhu, Yujin Cho, Qing He, Xiao Yang, Kevin Herrera, Zhaodong Chu, Yu Han, Michael C. Downer, Hailin Peng, and Keji Lai, “Out-of-plane piezoelectricity and ferroelectricity in layered α -In₂Se₃ nanoflakes,” *Nano Letters* **17**, 5508–5513 (2017).
- [11] Kai Chang, Junwei Liu, Haicheng Lin, Na Wang, Kun Zhao, Anmin Zhang, Feng Jin, Yong Zhong, Xiaopeng Hu, Wenhui Duan, Qingming Zhang, Liang Fu, Qi-Kun Xue, Xi Chen, and Shuai-Hua Ji, “Discovery of robust in-plane ferroelectricity in atomic-thick sn₂e,” *Science* **353**, 274–278 (2016).
- [12] Xiao Tang and Liangzhi Kou, “Two-dimensional ferroics and multiferroics: Platforms for new physics and applications,” *The Journal of Physical Chemistry Letters* **10**, 6634–6649 (2019).
- [13] Nicola A. Hill, “Why are there so few magnetic ferroelectrics?” *The Journal of Physical Chemistry B* **104**, 6694–6709 (2000).
- [14] Chao-Kai Li, Xu-Ping Yao, and Gang Chen, “Writing and deleting skyrmions with electric fields in a multiferroic heterostructure,” *Phys. Rev. Research* **3**, L012026 (2021).
- [15] Huai Yang, Longfei Pan, Mengqi Xiao, Jingzhi Fang, Yu Cui, and Zhongming Wei, “Iron-doping induced multiferroic in two-dimensional in₂se₃,” *Science China Materials* **63**, 421–428 (2020).
- [16] Xingen Liu, Alexander P. Pyatakov, and Wei Ren, “Magnetoelectric coupling in multiferroic bilayer vs₂,” *Phys. Rev. Lett.* **125**, 247601 (2020).
- [17] Jun-Jie Zhang, Lingfang Lin, Yang Zhang, Menghao Wu, Boris I. Yakobson, and Shuai Dong, “Type-ii multiferroic hf₂vc₂f₂ mxene monolayer with high transition temperature,” *Journal of the American Chemical Society* **140**, 9768–9773 (2018).
- [18] Jingshan Qi, Hua Wang, Xiaofang Chen, and Xiaofeng Qian, “Two-dimensional multiferroic semiconductors with coexisting ferroelectricity and ferromagnetism,” *Applied Physics Letters* **113**, 043102 (2018).
- [19] Changsong Xu, Peng Chen, Hengxin Tan, Yurong Yang, Hongjun Xiang, and L. Bellaiche, “Electric-field switching of magnetic topological charge in type-i multiferroics,” *Phys. Rev. Lett.* **125**, 037203 (2020).

- [20] Hengxin Tan, Menglei Li, Haitao Liu, Zhirong Liu, Yuanchang Li, and Wenhui Duan, “Two-dimensional ferromagnetic-ferroelectric multiferroics in violation of the d^0 rule,” *Phys. Rev. B* **99**, 195434 (2019).
- [21] I. Dzyaloshinsky, “A thermodynamic theory of “weak” ferromagnetism of antiferromagnetics,” *Journal of Physics and Chemistry of Solids* **4**, 241–255 (1958).
- [22] Tôru Moriya, “Anisotropic superexchange interaction and weak ferromagnetism,” *Phys. Rev.* **120**, 91–98 (1960).
- [23] Ning Ding, Jun Chen, Shuai Dong, and Alessandro Stroppa, “Ferroelectricity and ferromagnetism in a VO_2 monolayer: Role of the dzyaloshinskii-moriya interaction,” *Phys. Rev. B* **102**, 165129 (2020).
- [24] V. de Alfardo, S. Fubini, and G. Furlan, “A new classical solution of the yang-mills field equations,” *Phys Lett, B* **65**, 163–166 (Nov 1976).
- [25] Michael A. Susner, Marius Chyasnachyus, Michael A. McGuire, Panchapakesan Ganesh, and Petro Maksymovych, “Metal thio- and selenophosphates as multifunctional van der waals layered materials,” *Advanced Materials* **29**, 1602852 (2017).
- [26] Paolo Giannozzi *et al.*, “Quantum espresso: a modular and open-source software project for quantum simulations of materials,” *Journal of Physics: Condensed Matter* **21**, 395502 (2009).
- [27] P Giannozzi *et al.*, “Advanced capabilities for materials modelling with quantum espresso,” *Journal of Physics: Condensed Matter* **29**, 465901 (2017).
- [28] John P. Perdew, Kieron Burke, and Matthias Ernzerhof, “Generalized gradient approximation made simple,” *Phys. Rev. Lett.* **77**, 3865–3868 (1996).
- [29] Stefan Grimme, Jens Antony, Stephan Ehrlich, and Helge Krieg, “A consistent and accurate ab initio parametrization of density functional dispersion correction (dft-d) for the 94 elements h-pu,” *The Journal of Chemical Physics* **132**, 154104 (2010).
- [30] See Supplemental Material at [URL will be inserted by publisher] for more computational details, effects of electric fields or strain, phonon dispersions, magnetic parameters of the AFE-FM phase, and additional results of Monte-Carlo simulations. The supplemental material cite references[31–33].
- [31] M.J. van Setten, M. Giantomassi, E. Bousquet, M.J. Verstraete, D.R. Hamann, X. Gonze, and G.-M. Rignanese, “The pseudodojo: Training and grading a 85 element optimized norm-conserving pseudopotential table,” *Computer Physics Communications* **226**, 39–54 (2018).
- [32] John P. Perdew, Adrienn Ruzsinszky, Gábor I. Csonka, Oleg A. Vydrov, Gustavo E. Scuseria, Lucian A. Constantin, Xiaolan Zhou, and Kieron Burke, “Restoring the density-gradient expansion for exchange in solids and surfaces,” *Phys. Rev. Lett.* **100**, 136406 (2008).
- [33] Heather J. Kulik, Matteo Cococcioni, Damian A. Scherlis, and Nicola Marzari, “Density functional theory in transition-metal chemistry: A self-consistent hubbard u approach,” *Phys. Rev. Lett.* **97**, 103001 (2006).
- [34] Matteo Cococcioni and Stefano de Gironcoli, “Linear response approach to the calculation of the effective interaction parameters in the LDA + U method,” *Phys. Rev. B* **71**, 035105 (2005).
- [35] Koichi Momma and Fujio Izumi, “*VESTA3* for three-dimensional visualization of crystal, volumetric and morphology data,” *Journal of Applied Crystallography* **44**, 1272–1276 (2011).
- [36] Guy C. Moore, Matthew K. Horton, Alexander M. Ganose, Martin Siron, and Kristin A. Persson, “High-throughput determination of hubbard u and hund j values for transition metal oxides via linear response formalism,” (2022), [arXiv:2201.04213](https://arxiv.org/abs/2201.04213).
- [37] Chao Xu, Yancong Chen, Xiangbin Cai, Arno Meingast, Xuyun Guo, Fakun Wang, Ziyuan Lin, Tsz Wing Lo, Christian Maunders, Sorin Lazar, Ning Wang, Danguan Lei, Yang Chai, Tianyou Zhai, Xin Luo, and Ye Zhu, “Two-dimensional antiferroelectricity in nanostripe-ordered In_2Se_3 ,” *Phys. Rev. Lett.* **125**, 047601 (2020).
- [38] Andrius Dziaugys, Kyle Kelley, John A. Brehm, Lei Tao, Alexander Puretzy, Tianli Feng, Andrew O’Hara, Sabine Neumayer, Marius Chyasnachyus, Eugene A. Eliseev, Juras Banys, Yulian Vysochanskii, Feng Ye, Bryan C. Chakoumakos, Michael A. Susner, Michael A. McGuire, Sergei V. Kalinin, Panchapakesan Ganesh, Nina Balke, Sokrates T. Pantelides, Anna N. Morozovska, and Petro Maksymovych, “Piezoelectric domain walls in van der waals antiferroelectric $\text{CuIn}_2\text{P}_2\text{S}_6$,” *Nature Communications* **11**, 3623 (2020).
- [39] Hiroki Moriwake, Ayako Konishi, Takafumi Ogawa, Craig A. J. Fisher, Akihito Kuwabara, Kazuki Shitara, and Desheng Fu, “Polarization fluctuations in the perovskite-structured ferroelectric AgNbO_3 ,” *Phys. Rev. B* **97**, 224104 (2018).
- [40] Rohit Batra, Tran Doan Huan, Jacob L. Jones, George Rossetti, and Rampi Ramprasad, “Factors favoring ferroelectricity in hafnia: A first-principles computational study,” *The Journal of Physical Chemistry C* **121**, 4139–4145 (2017).
- [41] Yubo Qi, Sobhit Singh, Claudia Lau, Fei-Ting Huang, Xianghan Xu, Frederick J. Walker, Charles H. Ahn, Sang-Wook Cheong, and Karin M. Rabe, “Stabilization of competing ferroelectric phases of HfO_2 under epitaxial strain,” *Phys. Rev. Lett.* **125**, 257603 (2020).
- [42] Bheema Lingam Chittari, Youngju Park, Dongkyu Lee, Moonsup Han, Allan H. MacDonald, Euyheon Hwang, and Jeil Jung, “Electronic and magnetic properties of single-layer $m\text{PX}_3$ metal phosphorous trichalcogenides,” *Phys. Rev. B* **94**, 184428 (2016).
- [43] Stefan Grimme, “Semiempirical gga-type density functional constructed with a long-range dispersion correction,” *Journal of Computational Chemistry* **27**, 1787–1799 (2006).
- [44] A Togo and I Tanaka, “First principles phonon calculations in materials science,” *Scr. Mater.* **108**, 1–5 (2015).
- [45] R. D. King-Smith and David Vanderbilt, “Theory of polarization of crystalline solids,” *Phys. Rev. B* **47**, 1651–1654 (1993).
- [46] Graeme Henkelman and Hannes Jónsson, “Improved tangent estimate in the nudged elastic band method for finding minimum energy paths and saddle points,” *The Journal of Chemical Physics* **113**, 9978–9985 (2000).
- [47] Wenjun Ding, Jianbao Zhu, Zhe Wang, Yanfei Gao, Di Xiao, Yi Gu, Zhenyu Zhang, and Wenguang Zhu, “Prediction of intrinsic two-dimensional ferroelectrics in In_2Se_3 and other III 2 -VI 3 van der Waals materials,” *Nature Communications* **8** (2017).
- [48] John A. Brehm, Sabine M. Neumayer, Lei Tao, Andrew O’Hara, Marius Chyasnachyus, Michael A. Susner, Michael A. McGuire, Sergei V. Kalinin, Stephen Jesse, Panchapakesan Ganesh, Sokrates T. Pantelides, Petro

- Maksymovych, and Nina Balke, “Tunable quadruple-well ferroelectric van der waals crystals,” *Nature Materials* **19**, 43–48 (2020).
- [49] Sifan Xu, Zhicheng Wu, Yuriy S Dedkov, and Elena Voloshina, “Adsorption of water on the pristine and defective semiconducting 2d CrPX₃ monolayers (x: S, se),” *Journal of Physics: Condensed Matter* (2021).
- [50] Rui Gusmao, Zdenek Sofer, David Sedmidubsky, Stepan Huber, and Martin Pumera, “The role of the metal element in layered metal phosphorus triselenides upon their electrochemical sensing and energy applications,” *ACS Catalysis* **7**, 8159–8170 (2017).
- [51] Hongjun Xiang, Changhoon Lee, Hyun-Joo Koo, Xingao Gong, and Myung-Hwan Whangbo, “Magnetic properties and energy-mapping analysis,” *Dalton Trans.* **42**, 823–853 (2013).
- [52] N. D. Mermin and H. Wagner, “Absence of ferromagnetism or antiferromagnetism in one- or two-dimensional isotropic heisenberg models,” *Phys. Rev. Lett.* **17**, 1133–1136 (1966).
- [53] X. Z. Yu, W. Koshibae, Y. Tokunaga, K. Shibata, Y. Taguchi, N. Nagaosa, and Y. Tokura, “Transformation between meron and skyrmion topological spin textures in a chiral magnet,” *Nature* **564**, 95–98 (2018).
- [54] Gideon P. Müller, Markus Hoffmann, Constantin Dißelkamp, Daniel Schürhoff, Stefanos Mavros, Moritz Sallermann, Nikolai S. Kiselev, Hannes Jónsson, and Stefan Blügel, “Spirit: Multifunctional framework for atomistic spin simulations,” *Phys. Rev. B* **99**, 224414 (2019).
- [55] Xiaobo Lu, Ruixiang Fei, Linghan Zhu, and Li Yang, “Meron-like topological spin defects in monolayer crcl₃,” *Nature Communications* **11**, 4724 (2020).
- [56] Mathias Augustin, Sarah Jenkins, Richard F. L. Evans, Kostya S. Novoselov, and Elton J. G. Santos, “Properties and dynamics of meron topological spin textures in the two-dimensional magnet crcl₃,” *Nature Communications* **12**, 185 (2021).
- [57] N. Gao, S.-G. Je, M.-Y. Im, J. W. Choi, M. Yang, Q. Li, T. Y. Wang, S. Lee, H.-S. Han, K.-S. Lee, W. Chao, C. Hwang, J. Li, and Z. Q. Qiu, “Creation and annihilation of topological meron pairs in in-plane magnetized films,” *Nature Communications* **10**, 5603 (2019).
- [58] Manuel Pereiro, Dmitry Yudin, Jonathan Chico, Corina Etz, Olle Eriksson, and Anders Bergman, “Topological excitations in a kagome magnet,” *Nature Communications* **5**, 4815 (2014).

Supplementary Material for “Out-of-plane polarization and topological magnetic vortices in multiferroic CrPSe₃”

Weiwei Gao

*Key Laboratory of Materials Modification by Laser,
Ion and Electron Beams, Ministry of Education,
Dalian University of Technology, Dalian 116024, China and
Center for Computational Materials, Oden Institute for Computational Engineering and Sciences,
The University of Texas at Austin, Austin, TX 78712*

Jijun Zhao*

*Key Laboratory of Materials Modification by Laser,
Ion and Electron Beams, Ministry of Education,
Dalian University of Technology, Dalian 116024, China and
School of Physics, Dalian University of Technology*

James R. Chelikowsky†

*Center for Computational Materials, Oden Institute for Computational Engineering and Sciences,
The University of Texas at Austin, Austin, TX 78712
Department of Physics, The University of Texas at Austin, Austin, TX 78712 and
McKetta Department of Chemical Engineering, The University of Texas at Austin, Austin, TX 78712
(Dated: March 20, 2022)*

S1. COMPUTATION DETAILS

In this study, unit cells and several distinct supercells are used. In detail, we employed 20-atom rectangle supercells for structural relaxation of monolayer structures. For bulk structures having interlayer-antiferroelectric or interlayer-antiferromagnetic orders, we utilized 40-atom monoclinic supercells, while for other bulk phases, we used 20-atom supercells. The hexagonal primitive cell with 10 atoms is used to calculate the band structure of the ferroelectric-ferromagnetic phase. We investigated the convergence of our results to supercell sizes for phonon calculations using the frozen phonon approach, estimation of Hubbard U_{eff} using the linear response approach, and identification of magnetic exchange interactions. To separate periodic images of a monolayer, a vacuum region with a thickness of 15 Å is used. The Brillouin zone of the 20-atom monolayer unit cell is sampled using a $8 \times 5 \times 1$ k-point grid. Throughout the research, optimized norm-conserving pseudopotentials [1] and a kinetic energy cutoff of 80 Ryd are employed. For structural relaxations, we optimized both lattice vectors and atomic coordinates such that forces are less than 1×10^{-4} Ryd/Bohr and stresses are below 0.05 kbar. As illustrated in Table S1, we benchmarked different functionals for predicting the structure parameters for the centrosymmetric phase. Overall, PBEsol and LDA functional [2] outperforms PBE [3] and PBE+D3 [4]. When compared to LDA, PBEsol functional somewhat overestimates lattice constants, but gives better results of β and the ratios between lattice constants. We also noticed that as U_{eff} increases, the estimated lattice constants rise as well.

TABLE S1: Comparison between the structural parameters of the bulk centrosymmetric phase with the stripy arrangement calculated with different functionals. An effective Hubbard $U_{\text{eff}} = 3.6$ eV is used. Experimental data is from Ref [5].

Method	a (Å)	b (Å)	c (Å)	b/a	c/a	β	cell volume (Å ³)
LDA	6.18	10.84	6.80	1.754	1.100	108.4	434.8
PBE	6.37	11.15	7.15	1.750	1.122	108.0	485.6
PBE+D3	6.34	11.09	7.01	1.749	1.106	108.3	470.9
PBEsol	6.25	10.95	6.95	1.752	1.112	108.1	455.0
Experiment	6.13	10.66	6.86	1.739	1.119	107.1	428.4

*Electronic address: zhaojj@dlut.edu.cn

†Electronic address: jrc@utexas.edu

To get an reasonable estimate of U_{eff} , we used the linear response approach proposed by Cococcioni and Gironcoli [6] to estimate effective Hubbard U_{eff} parameters. The Hubbard $U_{\text{eff}}^{\text{out}}$ are determined using the ground state of PBEsol+ $U_{\text{eff}}^{\text{in}}$ calculations. We calculated Hubbard $U_{\text{eff}}^{\text{out}}$ for a series of $U_{\text{eff}}^{\text{in}}$, then perform linear extrapolation to get self-consistent U_{eff} parameters [7]. We have done convergence tests with respect to supercell size. Fig. S1 (a) suggests that a 40-atoms supercell is sufficient to converge the calculated U_{eff} within 50 meV. Comparing Fig. S1 (a) and (b), we found U_{eff} of FE and AFE phases are close (about 2.8 eV). Fig. S1 (c) demonstrates that PE-ST and PE-FM phase has the same self-consistent U_{eff} . In other words, U_{eff} is not sensitive to the magnetic order. We emphasize that U_{eff} is a model parameter which depends on the pseudopotentials. A recent high-throughput computational study by Guy et al. [8] show that 2.0 eV to 3.0 eV is a reasonable range of U_{eff} for Cr. This agrees well with what we find here, considering different methods we adopted.

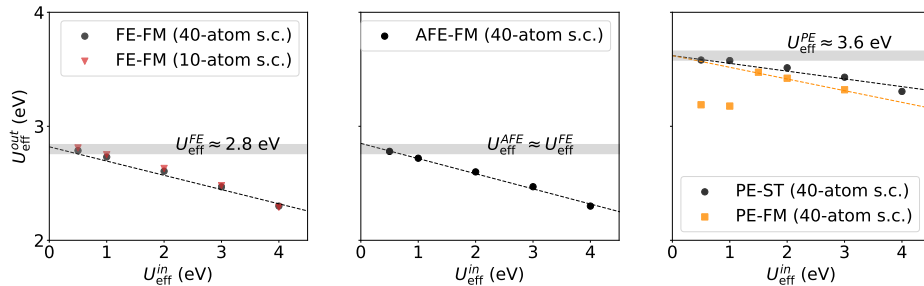


FIG. S1: Hubbard $U_{\text{eff}}^{\text{out}}$ versus input parameter $U_{\text{eff}}^{\text{in}}$ for PBEsol+ U_{eff} calculations. The self-consistent U_{eff} are highlighted as with horizontal lines.

S2. TOTAL ENERGIES OF MULTIFERROIC CONFIGURATIONS

We show the schematic plots of ferroelectric (FE), antiferroelectric (AFE), centrosymmetric (PE), and interlayer-antiferroelectric (iAFE) structures in Fig. S2. The total energies of different multiferroic configurations calculated with a range of U_{eff} parameters are presented in Table S2 and Table S3. We note that the exact energy differences between various phases can be dependent on the pseudopotential and exchange-correlation function used. For example, using LDA functional, we find the PE-ST, FE-FM, and AFE-FM phases have nearly the same energies when $U_{\text{eff}} = 3.0$, as shown in Table S4. Nevertheless, the overall trend discussed in the main text holds the same.

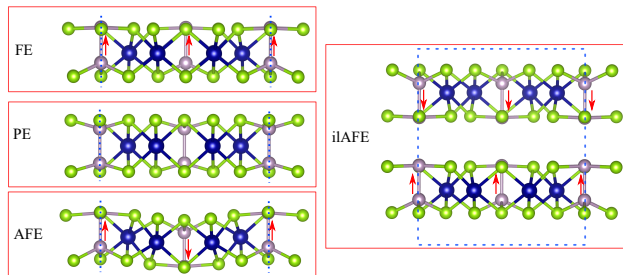


FIG. S2: Schematic plot of FE, PE, AFE, and iAFE structures.

TABLE S2: Total energies of monolayer configurations calculated with PBEsol+U using a range of Hubbard U_{eff} parameters. The energy of the FE-FM phase is set to zero. “-” means the calculations for corresponding structures do not converge (not local minima).

U_{eff} (eV)	FE (meV/f.u.)				AFE (meV/f.u.)				PE (meV/f.u.)			
	FM	ZZ	ST	NL	FM	ZZ	ST	NL	FM	ZZ	ST	NL
0.0	0	30	58	74	-14	4	6	26	125	152	230	-
2.0	0	44	64	83	-9	20	39	47	107	152	71	126
3.0	0	46	59	83	-3	25	48	50	-50	-8	-69	-31
3.6	0	50	-	82	7	31	58	56	-138	-99	-147	-116

TABLE S3: Total energies of different bulk configurations calculated with PBEsol+U using a range of Hubbard U_{eff} parameters. The energy of the FE-FM phase is set to zero. “-” means the calculations for corresponding structures do not converge.

U_{eff} (eV)	FE (meV/f.u.)					AFE (meV/f.u.)					PE (meV/f.u.)					ilAFE(meV/f.u.)				
	FM	ilAFM	ZZ	ST	NL	FM	ilAFM	ZZ	ST	NL	FM	ilAFM	ZZ	ST	NL	FM	ilAFM	ZZ	ST	NL
2.0	0	3	42	59	79	-16	-5	16	33	46	115	126	196	81	144	-8	-8	35	51	70
3.0	0	5	43	51	43	-11	-6	21	42	48	-41	-29	37	-59	-13	-7	-2	44	50	68
3.6	0	3	46	-	75	-4	-3	26	47	52	-129	-117	-52	-139	-100	-5	-2	48	-	71

TABLE S4: Comparison between the total energies of monolayer CrPSe₃ calculated with different functionals.

Method	PE-ST (meV/f.u.)	FE-FM (meV/f.u.)	AFE-FM (meV/f.u.)
PBEsol+U (U=3.0 eV)	0	69	66
LDA+U (U=3.0 eV)	0	6	3
LDA+U (U=2.9 eV)	0	-9	-11

S3. EFFECTS OF ELECTRIC FIELD AND STRAIN

We studied the effects of uniaxial strain and out-of-plane electric field E_z on the relative energy between AFE-FM and FE-FM phase. We found both strain and electric field can effectively tune the energy ordering between these two phases. As shown in Fig. S3 (a), an electric field of 1.7 V/nm perpendicular to the plane is sufficient to reverse the energy ordering between the AFE-FM and FE-FM phase. In Fig. S3 (b) and (c), we plot the strain dependent energies by changing lattice constant a and b . One can see small uniaxial strain (about 1.5 %) can make the energy of the AFE-FM phase higher than the FE-FM phase. These calculations are performed with PBEsol+U ($U_{\text{eff}} = 2.8$ eV).

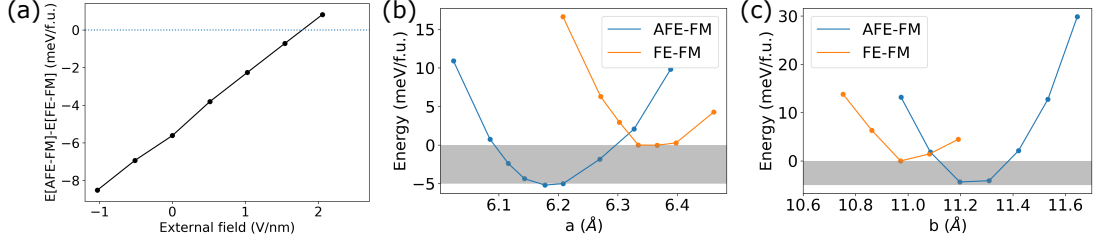


FIG. S3: (a) The energy difference between the AFE-FM phase and the FE-FM phase under electric field along out-of-plane direction. (b) and (c) Energies of the AFE-FM phase and FE-FM phase by changing lattice constant a and b .

S4. ELECTRON AND PHONON BAND STRUCTURES

The band structure of FE-FM and AFE-FM phases are shown in Fig. S4 (a) and (b). Interestingly, the band gaps of the FE-FM and AFE-FM phases both decrease as the effective Hubbard parameter U_{eff} parameter increases. The phonon band structure of the AFE-FM phase is plotted in Fig. S4 (c), which does not show any imaginary phonon modes. It demonstrates the dynamical stability of the AFE-FM phase.

The phonon spectra of monolayer PE-ST, monolayer PE-FE, and bulk PE-ST phase are shown in Fig. S5. Interestingly, all of them are stable without imaginary phonon modes. Usually, the corresponding PE structure of common FE materials should have imaginary phonon modes. The stability of PE phases is counterintuitive since our calculations show adding small distortions to PE phase can drive CrPSe₃ to the FE phase. To better understand such an unexpected result, we conducted further analysis. In detail, we calculate the projections (i.e., inner products) of zone-center phonon modes to the atomic displacements from the PE-FM to the FE-FM structure. We find four optical-phonon modes (two modes with A_{2u} symmetry and two modes with A_{1g} symmetry, shown in Fig. S5 (b)) that contribute significantly to the atomic displacements from the PE-FM structure to the FE-FM structure. These four phonon modes exhibit strong anharmonicity. The atomic displacements of these four zone-center modes are shown in Fig. S6.

Next, we calculated the energy landscape in the vicinity of the FE-FM and the PE-FM phase. In detail, we shifted the atoms by

$$\vec{d} = Q_1 \cdot (c_{A_{2u}[1]} \cdot \vec{u}_{A_{2u}[1]} + c_{A_{2u}[2]} \cdot \vec{u}_{A_{2u}[2]}) + Q_2 \cdot (c_{A_{1g}[1]} \cdot \vec{u}_{A_{1g}[1]} + c_{A_{1g}[2]} \cdot \vec{u}_{A_{1g}[2]})$$

$$c_{A_{2u}[1]} = 0.83; c_{A_{2u}[2]} = 0.11; c_{A_{1g}[1]} = -0.46; c_{A_{1g}[2]} = 0.21.$$

and calculate the energy of the distorted system $E(Q_1, Q_2)$. Here the \vec{u}_i is the eigenvector of phonon mode i and the coefficient c_i is calculated by projecting a phonon mode \vec{u}_i to the relative atomic displacements between the PE-FM and the FE-FM phase. For example, $\vec{u}_{A_{2u}[1]}$ is the eigenvector of phonon mode $A_{2u}[1]$. We plot the contour of $E(Q_1, Q_2)$ in Fig. S7, which clearly show three local minima. The PE-FM phase is located at a shallow local minimum in the center of Figure A5, while the FE phases correspond to the two other local minima. Fig. S7 suggests the PE-FM phase is metastable, however, adding small displacements to the PE-FM structure may cause a transition to the FE-FM phase. It also demonstrates the complexity of the energy landscape of CrPSe₃.

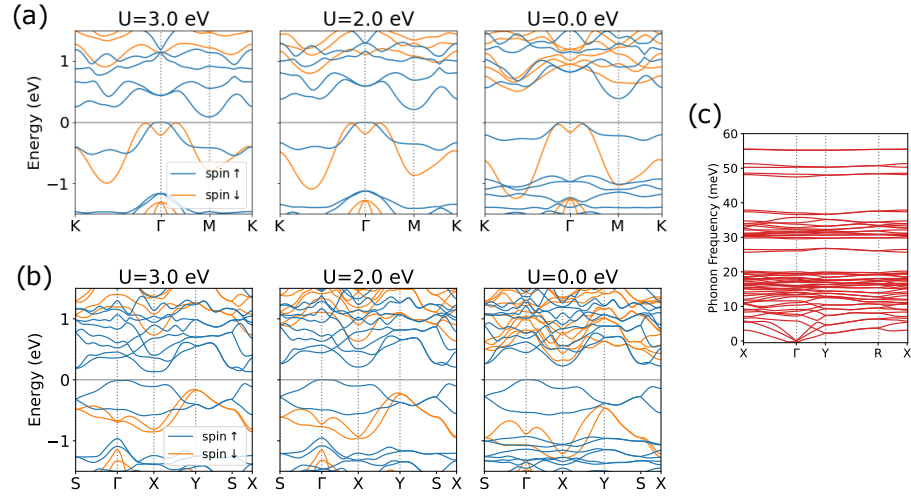


FIG. S4: Electron band structure of (a) the FE-FM and (b) AFE-FM phase calculated with different U_{eff} . (c) Phonon band structure of AFE-FM phase calculated with PBEsol+U ($U_{\text{eff}} = 2.8$ eV).

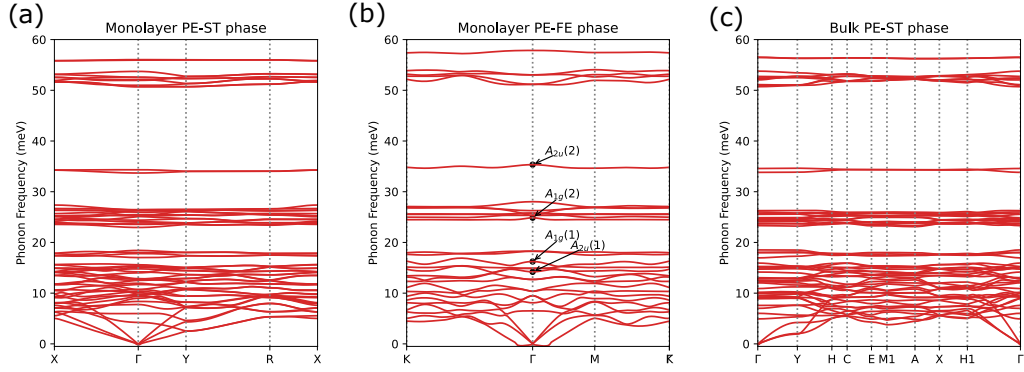


FIG. S5: Phonon band structure of (a) monolayer PE-ST (b) monolayer PE-FE (c) Bulk PE-ST phases, calculated with PBEsol+U.

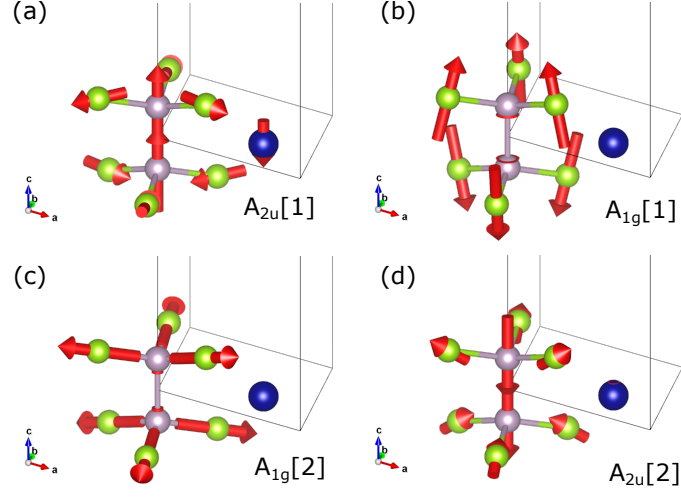


FIG. S6: Four phonon modes that contribute to the transition from the PE structure to the FE structure. Only a few atoms in the unit cell are shown for clarity.

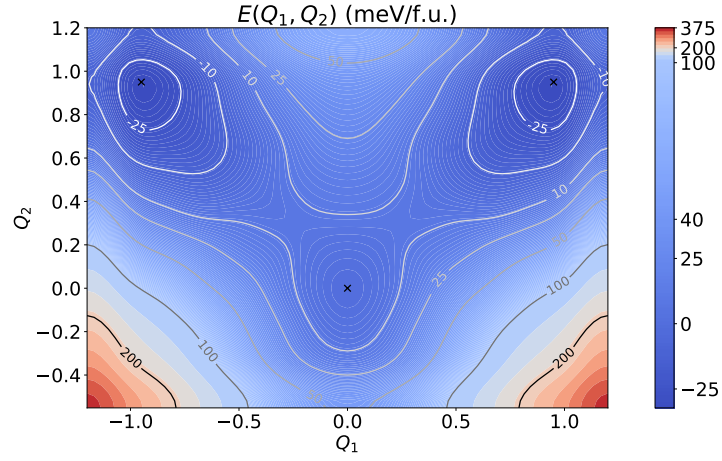


FIG. S7: The energy landscape near the PE-FM and FE-FM phase, showing three local minima. The top two minima correspond to the FE-FM phase. The shallow minima in the center corresponds to the PE-FM phase. The result is calculated with PBEsol+U ($U_{\text{eff}} = 2.0$ eV).

S5. MAGNETIC PARAMETERS OF THE AFE-FM PHASE

For the AFE phase, we considered exchange couplings between Cr atoms up to next-nearest neighbors and DMI between nearest neighbors. The calculated exchange parameters for AFE phase are shown in Table S5. The definitions of J_{kl} ($k = 1, 2$ and $l = a, b, c$) are schematically shown in Fig. S8. We can see although the nearest-neighbor couplings J_{1l} are all ferromagnetic, the coupling strength varies with respect to bonding directions. The AFE phase also demonstrates an easy-plane anisotropy. However, different from the FE phase, the AFE phase loses the C_3 symmetry and the magnetic moments prefer y -direction. In particular, the magnetic moments prefer to align along the y -direction. By estimating the DMI strength, we found the DMI coupling is significant only when the nearest-neighboring Cr pairs lie along the y -direction. This can be understood by examining the local inversion center or dihedral angles spanned by Cr pairs and the Se atoms connecting them, as we discussed in the main text. As shown in Fig. S8, we found $\angle \text{SeCr}_1\text{Cr}_0\text{Se} = 172^\circ$, while $\angle \text{SeCr}_2\text{Cr}_0\text{Se} = \angle \text{SeCr}_3\text{Cr}_0\text{Se} = 180^\circ$. This suggests $\text{SeCr}_2\text{Cr}_0\text{Se}$ ($\text{SeCr}_3\text{Cr}_0\text{Se}$) form a parallelogram, which have an inversion center and can not create DMI between Cr_2 and Cr_0 (Cr_3 and Cr_0).

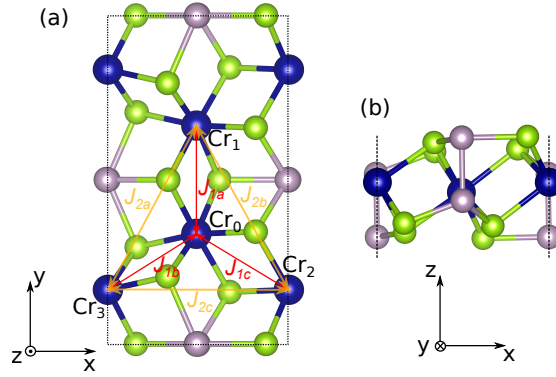


FIG. S8: (a) A schematic plot showing the definitions of exchange couplings between Cr in the AFE phase (b) A side view of the AFE structure

TABLE S5: Magnetic parameters (in meV) for the AFE phase.

J_{1a}	J_{1b}	J_{1c}	J_{2a}	J_{2b}	J_{2c}	D_{1a}	A_x	A_y
-8.7	-29.2	-8.8	-3.2	-2.6	-6.2	[-0.65,0,-0.5]	-0.07	-0.15

S6. MONTE CARLO SIMULATIONS

For Monte-Carlo (MC) simulations of the FE-FM phase, we used a 200×200 spin lattice, which includes 8×10^4 spin sites. In order to observe the evolution of meron and antimerons, we performed MC simulation up to 10^6 MC steps for each temperature. We used a modified version of Spirit [9]. For a continuous unit vector field $\mathbf{n}(\mathbf{r})$ on a plane, the topological charge is defined as

$$Q[\mathbf{n}(\mathbf{r})] = \frac{1}{4\pi} \int_{\mathbb{R}^2} \mathbf{n} \cdot (\partial_x \mathbf{n} \times \partial_y \mathbf{n}) d^2 \mathbf{r} \quad (1)$$

In comparison, for unit vector fields on a discrete 2D lattice, the topological charge is given by

$$Q = \frac{1}{4\pi} \sum_l A_l \quad (2)$$

where l runs over all the triangles of a triangulation of the spin lattice sites and A_l can be recognized as the local topological charge, which is

$$\cos\left(\frac{A_l}{2}\right) = \frac{1 + \mathbf{n}_i \cdot \mathbf{n}_j + \mathbf{n}_i \cdot \mathbf{n}_k + \mathbf{n}_j \cdot \mathbf{n}_k}{\sqrt{2(1 + \mathbf{n}_i \cdot \mathbf{n}_j)(1 + \mathbf{n}_j \cdot \mathbf{n}_k)(1 + \mathbf{n}_k \cdot \mathbf{n}_i)}}. \quad (3)$$

The spin sites i , j , and k of a triangle l are numbered in a counter-clockwise order. The sign of A_l is $\text{sign}[\mathbf{n}_i \cdot (\mathbf{n}_j \times \mathbf{n}_k)]$.

In Fig. S9, we show some screenshots of the spin lattice under $T = 5$ K. At MC step 50000, there are 7 pairs of merons (or antimerons). As the simulation goes, vortex and antivortex attract and annihilate each other. At MC step 500000, only one pair of merons left. We observed meron-meron, meron-antimeron, and antimeron-antimeron annihilation in our simulations. This indicates the pair annihilation processes do not depend on the polarity (the z component of the core) of merons (or antimerons).

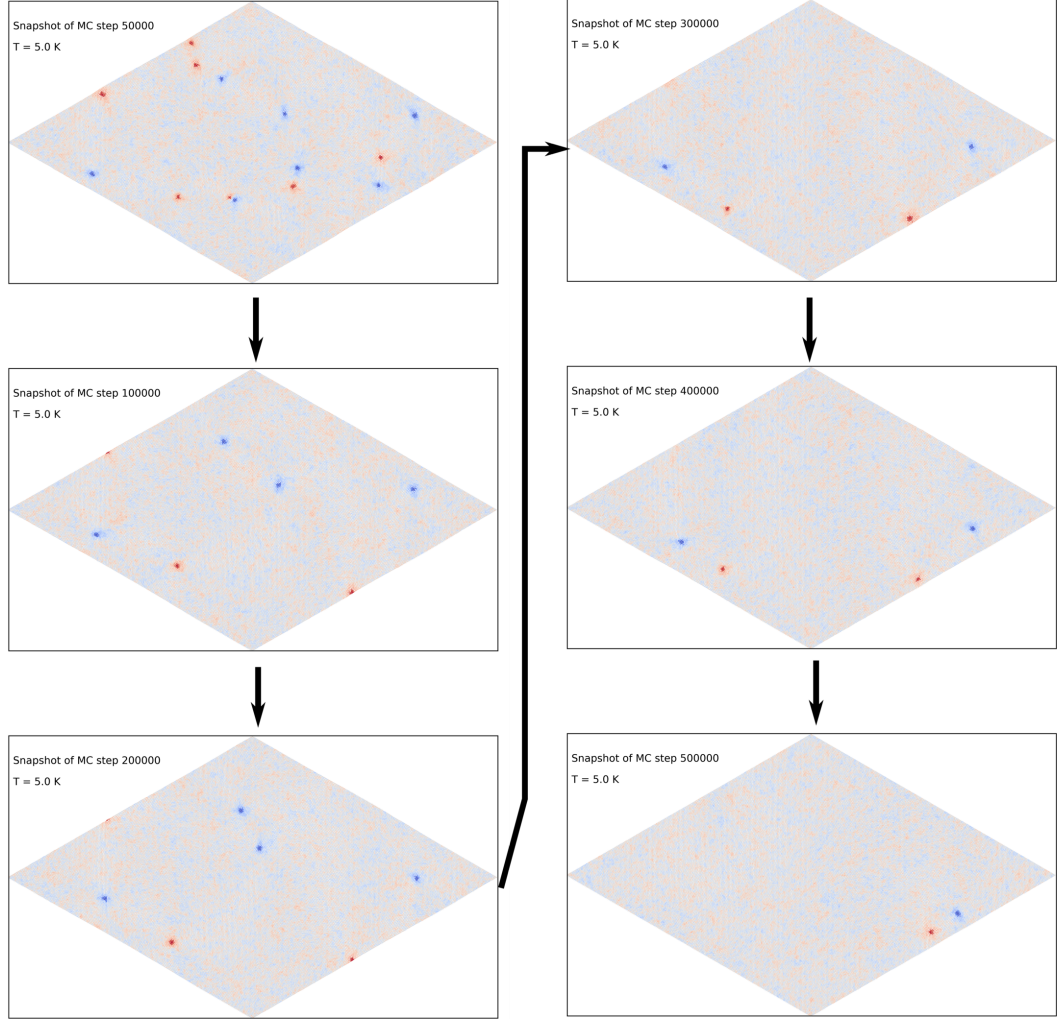


FIG. S9: Selected steps in the MC simulation of FE-FM phase at $T = 5$ K. The spins are colored in red or blue according to their z -components of magnetic moments.

We also performed MC calculations for the AFE-FM phase using a spin lattice with 80000 spin sites. The initial spin configurations were set to either randomized spin directions or out-of-plane ferromagnetic (zFM) configurations. Our calculations show only randomized initial spin configurations can yield merons in MC simulations. The zFM initial spin configuration only yields in-plane ferromagnetic domains with topological trivial domain boundaries. This is in contrast with the FE-FM phase, where MC simulations with zFM initial configuration also produce merons. In Fig. S10, we show typical screenshots of a MC simulation for the AFE-FM phase starting with a randomized initial spin configuration. Vortex and anti-vortex merons are observed. Compared to the FE-FM phase, the size of merons are larger. Furthermore, we observed some stable meron pairs showing long lifetimes in MC simulations. For example, Fig. S11 shows some pairs of vortex and antivortex merons stabilized at the upper domain boundary between two FM domains. Interestingly, four meron pairs on the upper boundary (marked with green rectangle boxes) do not show the tendency of annihilating each other after 2×10^6 MC steps.

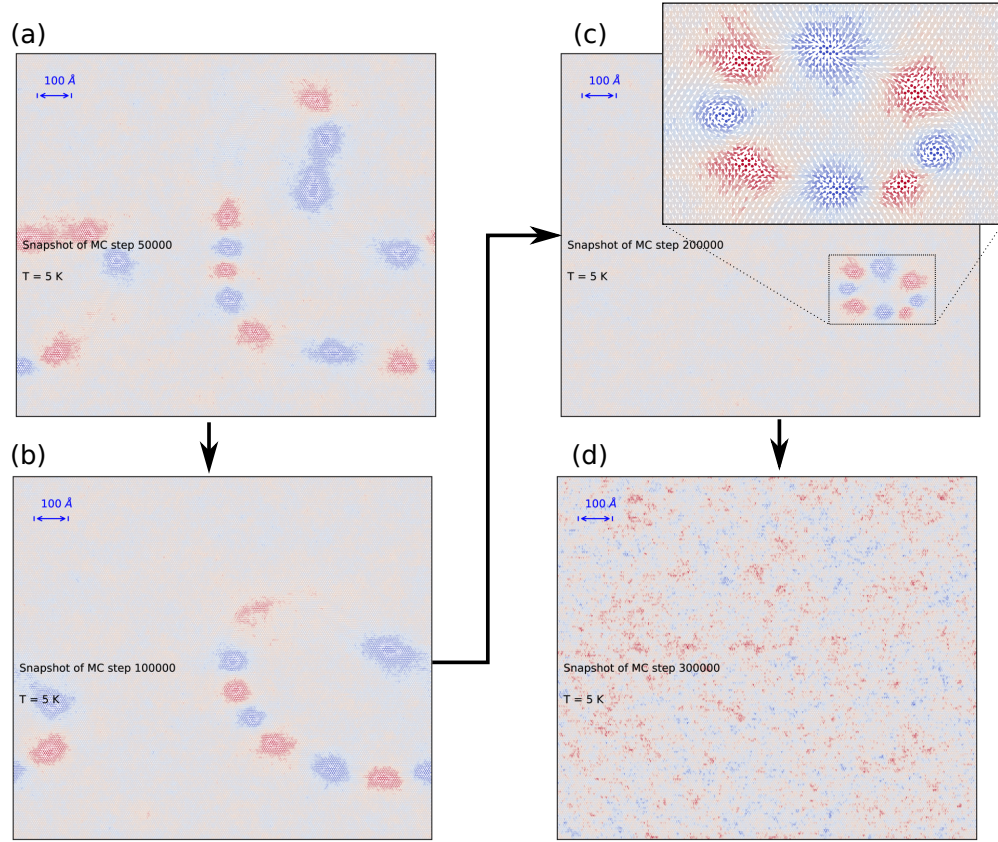


FIG. S10: Selected snapshots of the MC simulation of AFE-FM phase at $T = 5K$. The spins are colored in red or blue according to their z -components of magnetic moments. After 300000 MC steps, the spin lattice becomes a single ferromagnetic domain with magnetic moments pointing along negative y -direction.

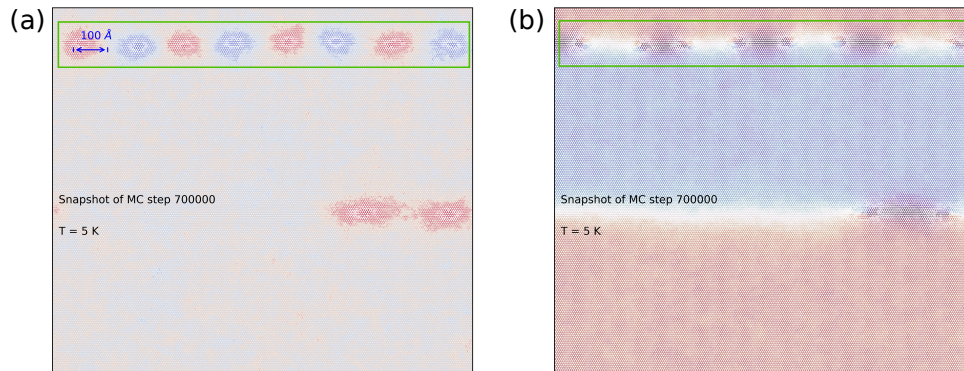


FIG. S11: A snapshot of the MC simulation of AFE-FM phase at $T = 5K$. The spins are colored according to their (a) z -components and (b) y -components of magnetic moments .

-
- [1] M. van Setten, M. Giantomassi, E. Bousquet, M. Verstraete, D. Hamann, X. Gonze, and G.-M. Rignanese, *Computer Physics Communications* **226**, 39 (2018).
 - [2] J. P. Perdew, A. Ruzsinszky, G. I. Csonka, O. A. Vydrov, G. E. Scuseria, L. A. Constantin, X. Zhou, and K. Burke, *Phys. Rev. Lett.* **100**, 136406 (2008).
 - [3] J. P. Perdew, K. Burke, and M. Ernzerhof, *Phys. Rev. Lett.* **77**, 3865 (1996).
 - [4] S. Grimme, J. Antony, S. Ehrlich, and H. Krieg, *The Journal of Chemical Physics* **132**, 154104 (2010).
 - [5] M. A. Susner, M. Chyashavichyus, M. A. McGuire, P. Ganesh, and P. Maksymovych, *Advanced Materials* **29**, 1602852 (2017).
 - [6] M. Cococcioni and S. de Gironcoli, *Phys. Rev. B* **71**, 035105 (2005).
 - [7] H. J. Kulik, M. Cococcioni, D. A. Scherlis, and N. Marzari, *Phys. Rev. Lett.* **97**, 103001 (2006).
 - [8] G. C. Moore, M. K. Horton, A. M. Ganose, M. Siron, and K. A. Persson, “High-throughput determination of hubbard u and hund j values for transition metal oxides via linear response formalism,” (2022), [arXiv:2201.04213](https://arxiv.org/abs/2201.04213) .
 - [9] G. P. Müller, M. Hoffmann, C. Dißelkamp, D. Schürhoff, S. Mavros, M. Sallermann, N. S. Kiselev, H. Jónsson, and S. Blügel, *Phys. Rev. B* **99**, 224414 (2019).